This is a "preproof" accepted article for *Mineralogical Magazine*.
This version may be subject to change during the production process.
10.1180/mgm.2025.3

Discovery of terrestrial rubinite, $Ca_3Ti^{3+}_2Si_3O_{12}$, super-reduced garnet from the Hatrurim Complex, Israel

Evgeny V. Galuskin[1]*, Irina O. Galuskina[1], Joachim Kusz[2], Yevgeny Vapnik[3] and Grzegorz Zieliński[4]

[1]Institute of Earth Sciences, Faculty of Natural Sciences, University of Silesia, Będzińska 60, 41-200 Sosnowiec, Poland

[2]Faculty of Science and Technology, University of Silesia, 75. Pułku Piechoty 1, 41-500 Chorzów, Poland

[3]Department of Geological and Environmental Sciences, Ben-Gurion University of the Negev, P.O.B. 653, Beer-Sheva 84105, Israel

[4]Polish Geological Institute – National Research Institute, Rakowiecka 4, 00-975 Warsaw, Poland.

*E-mail: evgeny.galuskin@us.edu.pl

Abstract

Rubinite, a garnet with the ideal formula $Ca_3Ti^{3+}_2Si_3O_{12}$, is an indicator of super-reduced conditions and has recently been found in refractory inclusions in a few CV3 chondrites. We discovered rubinite in phosphide-bearing breccia from the pyrometamorphic Hatrurim Complex, Negev Desert, Israel. Aggregates of phosphide and native iron are concentrated at the boundary of thermally altered sedimentary xenoliths encased in flamite-gehlenite paralava. Rubinite, with the average empirical formula $(Ca_{2.97}Mg_{0.02}Fe^{2+}_{0.01})_{\sum 3.00}$ $(Ti^{3+}_{1.10}Al_{0.44}Ti^{4+}_{0.37}Mg_{0.08}Cr_{0.01})_{\sum 2}(Si_{2.71}Al_{0.29})_{\sum 3.00}O_{12}$, was found in a small xenolith composed of hydrogrossular, tacharanite and calcite, and containing relics of high-temperature minerals such as pseudowollastonite, cuspidine, gehlenite, baghdadite, barringerite, murashkoite, osbornite, paqueite and oldhamite.

https://doi.org/10.1180/mgm.2025.3 Published online by Cambridge University Press

For the first time, a structure of rubinite, with the composition $(Ca_{2.99}Mg_{0.01})_{\Sigma 3}(Ti^{3+}_{0.78}Al_{0.62}\,Ti^{4+}_{0.43}Mg_{0.17})_{\Sigma 2}(Si_{2.74}\,Al_{0.26})_{\Sigma 3}O_{12}$, has been refined. Its unit-cell parameter a = 12.0193(4)Å, is significantly smaller than that of the synthetic analogue of $Ca_3Ti_2Si_3O_{12}$, 12.1875Å. In a Raman spectrum of rubinite weak bands corresponding to the vibrations of Ti^{4+}-O in the $(TiO_6)^{8-}$ octahedra: 610 cm^{-1} $\nu_1(TiO_6)^{8-}$ and 438 cm^{-1} $\nu_4(TiO_6)^{8-}$ are present in addition to the bands related to Si-O and Al-O vibrations in the TO_4 tetrahedra. Rubinite forms a thin reactive rim (<10 μm) on pseudowollastonite grains. It likely formed during a sharp increase in rock porosity in the course of natural clinkerisation of sedimentary xenoliths caused by the thermal impact of the paralava. The high porosity increased the effect of reductive gases on the rocks, which were by-products of pyrometamorphism. The brief appearance of super-reduced conditions defined the formation of the Ti^{3+}-bearing minerals osbornite and rubinite. Paqueite, $Ca_3Ti^{4+}(Ti^{4+}Al_2)Si_2O_{14}$, which crystallized in a thin melting zone of xenolith at the boundary with the paralava, does not contain Ti^{3+}.

Keywords: garnet, rubinite, structure, terrestrial rock, Raman, paralava, super-reduced minerals, Hatrurim Complex, Israel

Introduction

In 2013, nomenclature of the garnet supergroup, in which 32 mineral species were described, was published by Grew *et al*.. There are currently about 40 mineral species in the garnet supergroup. The rarest natural garnet, rubinite, was discovered in refractory inclusions in CV3 chondrites (Vigarano, Allende and Efremovka) in 2015 and has the ideal formula $Ca_3Ti^{3+}_2Si_3O_{12}$ (Ma *et al*., 2024). It is considered to be one of the earliest minerals formed in the solar nebula.

Minerals in which titanium has a valence of less than 4+ are considered to be indicators of super-reduced conditions. At terrestrial sites, the discovery of minerals containing trivalent titanium (carmeltazite, magnéliite, sassite, tistarite and others) is mainly related to the study of inclusions in corundum from heavy fractions (separates) that were most likely contaminated by anthropogenic material (Griffin *et al*., 2016; Bindi *et al*., 2018; Litasov *et al*., 2019; Balhaus *et al*., 2021; Galuskin and Galuskina, 2023a, b).

There are rare finds of super-reduced minerals in situ in terrestrial rocks, where there is no doubt as to their natural origin. One example is osbornite, TiN, found in a phosphide-

https://doi.org/10.1180/mgm.2025.3 Published online by Cambridge University Press

bearing breccia from a small outcrop of pyrometamorphic rocks of the Hatrurim Complex in the Negev Desert, Israel (Galuskin *et al*., 2022). Rubinite was found in a single sample of the same breccia in association with osbornite. Rubinite completes the list of the garnet supergroup minerals found in the pyrometamorphic rocks of the Hatrurim Complex. Thus, garnets of the andradite-schorlomite-grossular series, often with significant admixture of Cr and V, are most common in gehlenite hornfels and wollastonite-rankinite paralavas (Krzątała *et al*., 2020). The pyrometamorphic rocks of the Hatrurim Complex are the type localities of two new garnets: priscillagrewite, $(Ca_2Y)Zr_2Al_3O_{12}$, found in fluorapatite-spurrite marbles, Daba Siwaqa, Jordan (Galuskina *et al*., 2021) and midbarite, $Ca_3Mg_2(V^{5+}{}_2Si)O_{12}$, found in gehlenite paralava, Hatrurim Basin, Israel (Galuskina *et al*., 2024). In addition, garnets of the kerimasite-kimzeite series, $Ca_3Zr_2Fe^{3+}{}_2SiO_{12}$ - $Ca_3Zr_2Al_2SiO_{12}$, an Al-analogue of elbrusite corresponding to the composition series $Ca_3(Zr_{1.5}U^{6+}{}_{0.5})Al_3O_{12}$ - $Ca_3ZrU^{5+}Al_3O_{12}$ (Galuskina *et al*., 2015) and an analogue of midbarite with Mn^{2+}>Mg were found in single cases. Garnets of the grossular-katoite series are widespread in the low-temperature alteration products of the pyrometamorphic rocks of the Hatrurim Complex (Kruszewski *et al*., 2021). All of the above-mentioned garnets are characteristic of oxidised mineral associations of rocks of the Hatrurim Complex, whereas finds of garnets in reduced associations, as in the case of rubinite, are rare. For example, Fe-free Ti-V-bearing uvarovite has been found in wollastonite-gehlenite paralava with large inclusions of native iron up to 1 cm, crystallized under reduced conditions near the iron-wüstite buffer (Futrzyński *et al*., 2023).

In this paper, we present the results of a study of the morphology and composition of rubinite and associated minerals, and provide the results of single-crystal structural and Raman studies of rubinite. We also discuss the conditions and growth mechanism of rubinite, which reflect the formation of the mineral under super-reduced conditions at the Earth's surface.

Methods of investigation

The morphology and composition of rubinite and associated minerals were studied using an Olympus optical microscope, a Quanta 250 scanning electron microscope with UltraDry EDS Detector (Institute of Earth Sciences, Faculty of Natural Sciences, University of Silesia, Sosnowiec, Poland) and an electron probe microanalyser (Cameca SX100, Micro-Area Analysis Laboratory, Polish Geological Institute - National Research Institute, Warsaw, Poland). Chemical analyses were carried out in WDS mode (wavelength-dispersive X-ray spectroscopy, settings: 15 keV, 20 nA and ~1 μm beam diameter) using the synthetic and

https://doi.org/10.1180/mgm.2025.3 Published online by Cambridge University Press

natural standards: Mg*K*α – diopside; Si*K*α and Zr*L*α – zircon; Al*K*α and K*K*α – orthoclase; Ca*K*α – wollastonite; Sr*L*α – celestine; Nb*L*α – metallic Nb; Ba*L*β – baryte; Ti*K*α – rutile; V*K*α – metallic V; Cr*K*α – Cr_2O_3; P*K*α and F*K*α – fluorapatite; Mn*K*α – rhodonite; Fe*K*α – pentlandite; and Cl*K*α – tugtupite. Elemental EDS analysis of minerals was performed using a routine procedure with internal standards, ZAF correction and 100% normalization of totals.

The single-crystal X-ray study of a rubinite crystal was carried out using a SuperNova diffractometer with a mirror monochromator (Cu*K*α, λ = 1.54184 Å) and an Atlas CCD detector (Agilent Technologies) at the Institute of Physics, University of Silesia, Poland. The structure of rubinite was refined using the SHELX-2019/2 program (Sheldrick, 2015). The crystal structure was refined starting from the atomic coordinates of uvarovite (Futrzyński *et al*., 2023).

The Raman spectrum of rubinite was recorded on a WITec alpha 300R Confocal Raman Microscope (Department of Earth Science, University of Silesia, Poland) equipped with an air-cooled solid laser (488 nm) and a CCD camera operating at -61°C. An air Zeiss LD EC Epiplan-Neofluan DIC-100/0.75NA objective was used. Raman scattered light was focused onto a multi-mode fiber and monochromator with a 1,800 mm^{-1} grating. The power of the laser at the sample position was ~40 mW. Fifteen scans with an integration time of 3 s and a resolution of ~3 cm^{-1} were collected and averaged. The spectrometer monochromator was calibrated using the Raman scattering line of a silicon plate (520.7 cm^{-1}).

Occurrence

Rubinite was found in a single sample of the phosphide-bearing breccia of the Hatrurim Complex, which was discovered in 2019 as a small vertical zone 4–5 meters thick in an exposure created during the construction of the Arad – Dead Sea road (Galuskin *et al*., 2022, 2023a). The results of this breccia investigation can be found in our papers describing findings of 'meteoritic minerals' such as osbornite, barringerite and schreibersite (Galuskin *et al*., 2022), andreyivanovite and allabogdanite (Galuskin *et al*., 2023a), and caswellsilverite and grokhovskyite (Galuskin *et al*., 2023b). In the breccia, xenoliths of altered sedimentary rocks ranging in size from a few centimeters to 0.5 m, cemented by flamite-gehlenite (± rankinite, pseudowollastonite) paralava, usually have a characteristic zonation. The contact facies of black gehlenite-flamite or gehlenite-rankinite amygdaloidal paralava (zone 1) is represented by a light pseudowollastonite-gehlenite zone 2-3 mm thick, intensely replaced by OH-bearing grossular (hydrogrossular) and hydrous silicates (zone 2) (Fig. 1a). This thin zone

reflects the effect of contamination of the carbonate xenolith material by the paralava, which is expressed as an increase in the Ca/Si ratio. Contamination led to the formation of pseudowollastonite in the paralava. At the contact with the paralava, the xenolith itself often has a thin zone several millimeters thick, which usually differs in colour (zone 3) from the central parts of the xenolith (zone 4, Fig. 1a). This zone is interpreted by us as a zone of almost complete melting (Galuskin *et al*., 2022). Rubinite was only found where the zones described are unevenly developed (Fig. 1b).

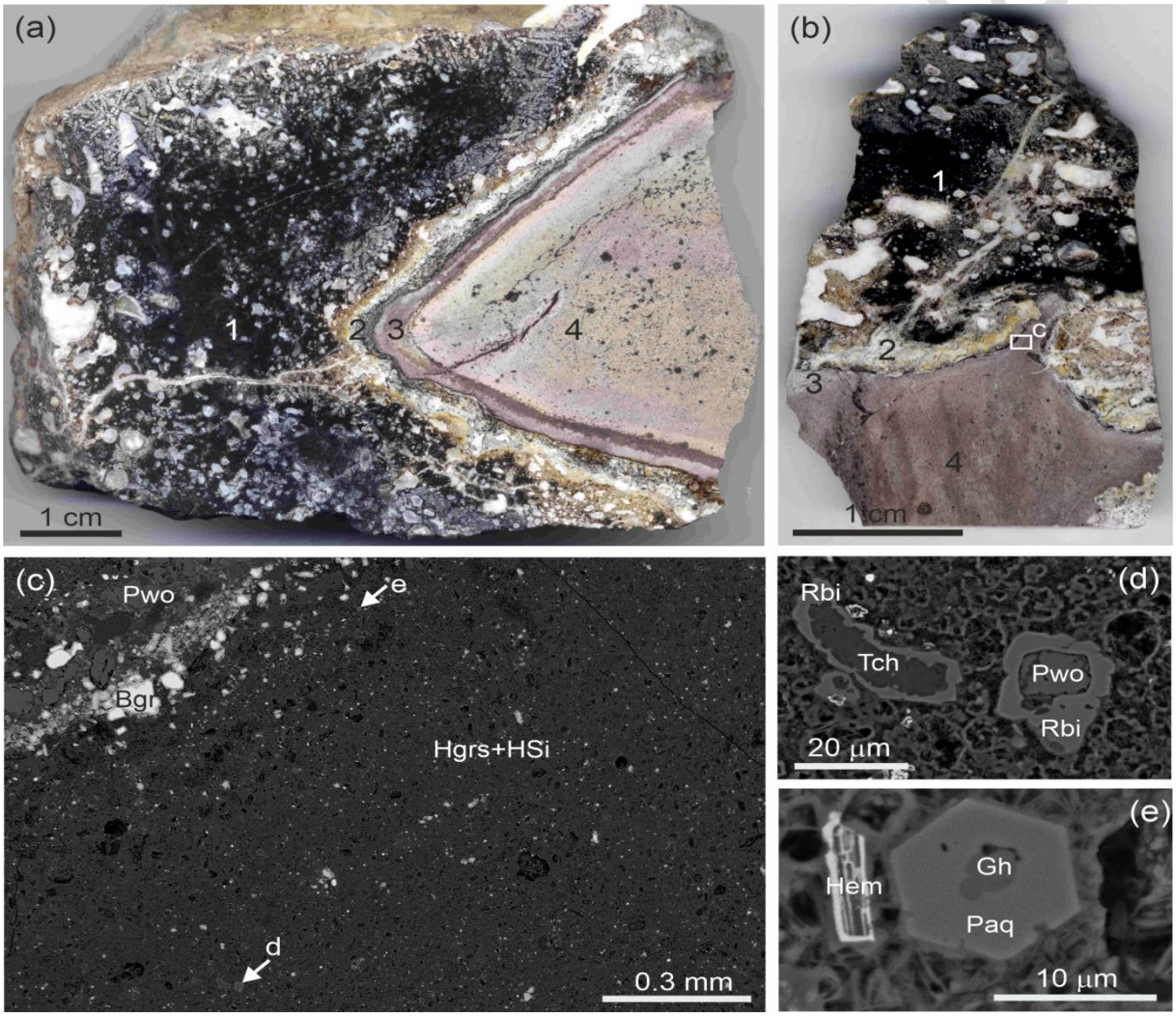

Figure 1. (a) Typical zonation of breccia: 1 – gehlenite-flamite-rankinite paralava, 2 - pseudowollastonite-bearing paralava contaminated by xenolith material, 3 – altered hematite-bearing xenolith melting zone, 4 – altered hematite-bearing xenolith thermal alteration zone. (b) General view of sample with rubinite, frame outlines a fragments enlarged in Fig. 1c. 1 – 4 – Zones as in Fig. 1A. (c) Contact of xenolith with paralava. Fragments magnified in Fig. 1d,f are indicated by arrows. (d) Typical zonal aggregates of rubinite from zone 4. (e) Paqueite crystal with gehlenite inclusions from zone 3, nearby secondary hematite replaces troilite. (c-e) – BSE images. Bgr = barringerite, Gh = gehlenite, Hem = hematite, Hgrs = hydrogrossular, HSi = hydrosilicates, Paq =paqueite, Pwo = pseudowollastonite, Rbi = rubinite, Tch = tacharanite.

https://doi.org/10.1180/mgm.2025.3 Published online by Cambridge University Press

This xenolith, like most xenoliths of phosphide-bearing breccias, consists of hydrogrossular, calcium hydrosilicates (predominantly tacharanite) and calcite; in some fragments the rock is enriched in gypsum, ettringite, whewellite and halite (Fig. 2). Relict high-temperature minerals are represented by small grains of barringerite, murashkoite, perovskite, baghdadite, pseudowollastonite, cuspidine, osbornite, paqueite, fluorapatite, oldhamite and, rarely, gehlenite (Galuskin *et al.*, 2022). In the porous rock of the xenoliths, case-like hydrogarnet pseudomorphs are widespread (Fig. 2a,b), the morphology of which indicates that clasts of clay-carbonate sedimentary rock (Ghareb Formation) were transformed at temperatures >1,200°C into a gehlenite-hatrurite (+ CaO, CaS) clinker-like rock, which was later completely altered by low-temperature processes. The detection of circular forms, in some cases with inscribed rectangles (Fig. 2c,d), indicates the formation of melt droplets during clinkerisation.

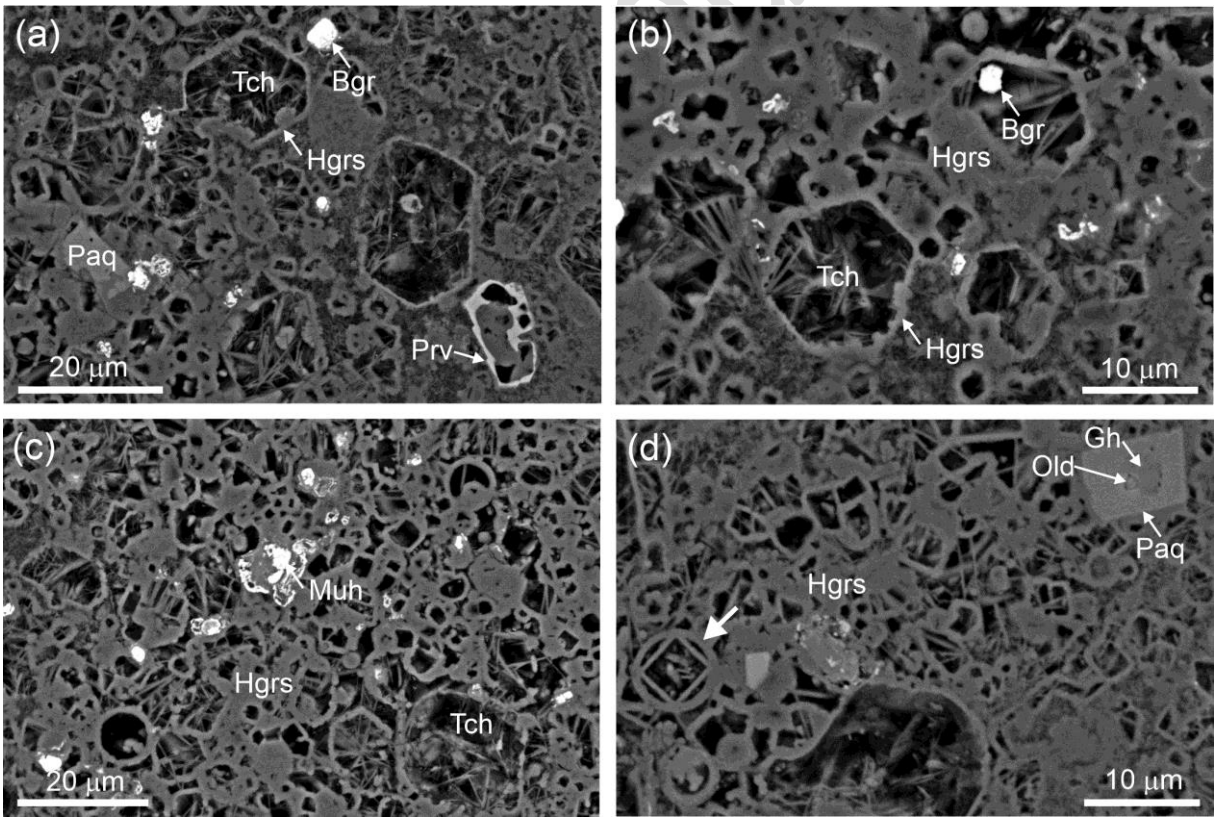

Figure 2. (a, b) Hexagonal case-like pseudomorphs of hydrogrossular after hatrurite. (c, d) Rounded and rectangular case-like forms of pseudomorphs after hatrurite, gehlenite and melt drops. Bgr = barringerite, Gh = gehlenite, BSE images. Hgrs = hydrogrossular, Muh = murashkoite, Old = oldhamite, Paq = paqueite, Prv = perovskite, Tch = tacharanite.

https://doi.org/10.1180/mgm.2025.3 Published online by Cambridge University Press

Numerous grains of rubinite, whose composition is described by the simplified formula $Ca_3(Ti^{3+},Al,Ti^{4+},Mg)_2(Si,Al)_3O_{12}$, occur in zone 4 of the xenolith, whereas paqueite crystals of similar composition – $Ca_3Ti^{4+}(Al,Ti^{4+},Si)_3Si_2O_{14}$ – are characteristic of zone 3 (Fig. 1c-f, 3a). Rubinite forms aggregates with relics of pseudowollastonite in the central part of the crystals and rarely forms single crystals (Fig. 3b-d, 4). Reaction rims of rubinite on pseudowollastonite up to 10 μm thick appear as an eyed structure (Fig. 3c, 4a,c,e), which is particularly visible in optical images where the light core of pseudowollastonite is surrounded by grey-brown rubinite, in some cases with a greenish tinge (Fig. 3d, 4d,f).

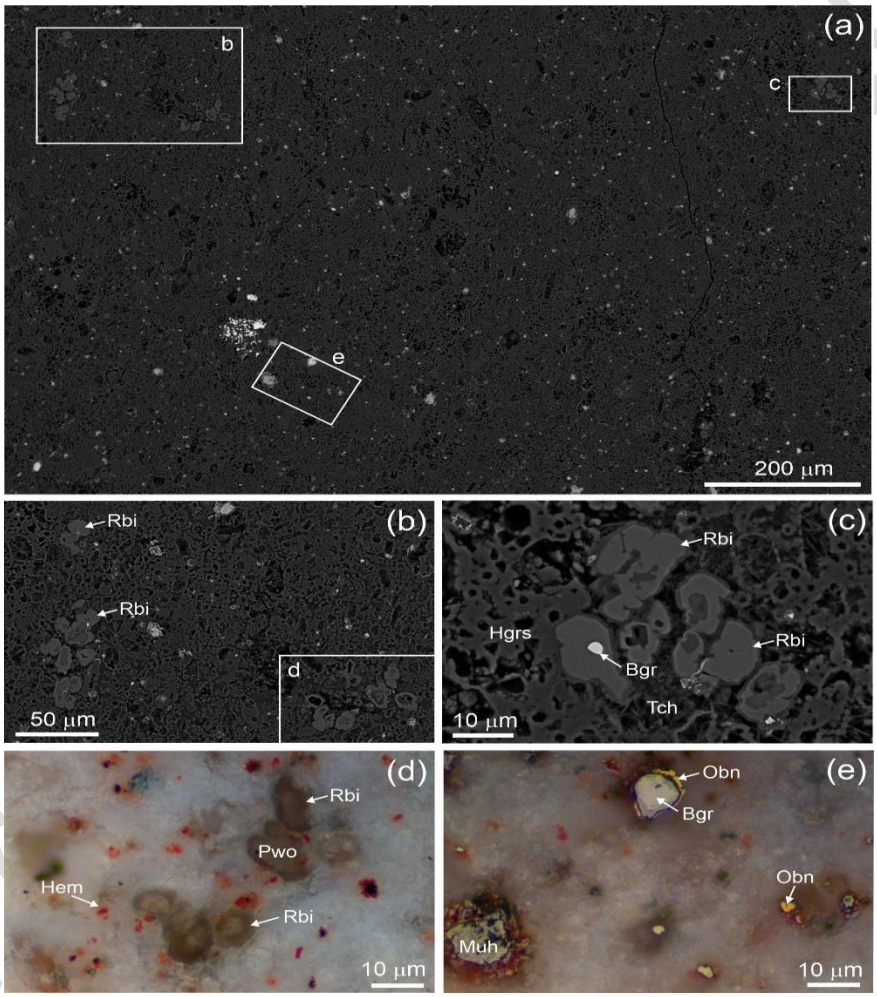

Figure 3. (a) Central part of a xenolith represented by porous aggregates of hydrogrossular, tacharanite, calcite and gypsum, in some cases enriched with halite. Relict inclusions of high-temperature minerals are represented by rubinite, perovskite, pseudowollastonite, barringerite, murashkoite, and osbornite. Magnified fragments in Figs. 3b-d are shown in frames. (b) Zonal aggregates, the centre of which is filled by pseudowollastonite and/or products of its alteration, and the rim consist of by rubinite. (c) Aggregates of rubinite crystals with barringerite inclusions and clearly visible {221} and {110} faces. (d) Rubinite rims on pseudowollastonite. (e) Osbornite usually forms rims on barringerite. a-c – BSE, d, e – optical images, reflected light, d – XPL, e – PPL. Bgr = barringerite, Hgrs = hydrogrossular, Hem = hematite, Muh = murashkoite, Obn = osbornite, Pwo = pseudowollastonite, Rbi = rubinite, Tch = tacharanite.

https://doi.org/10.1180/mgm.2025.3 Published online by Cambridge University Press

Rare inclusions of gehlenite and barringerite are found in rubinite crystals (Fig. 3c, 4a,e). Rubinite grains exhibit {211} and {110} faces (Fig. 4a,b,e). Associated with rubinite, osbornite forms a rim on barringerite (Fig. 3a,e).

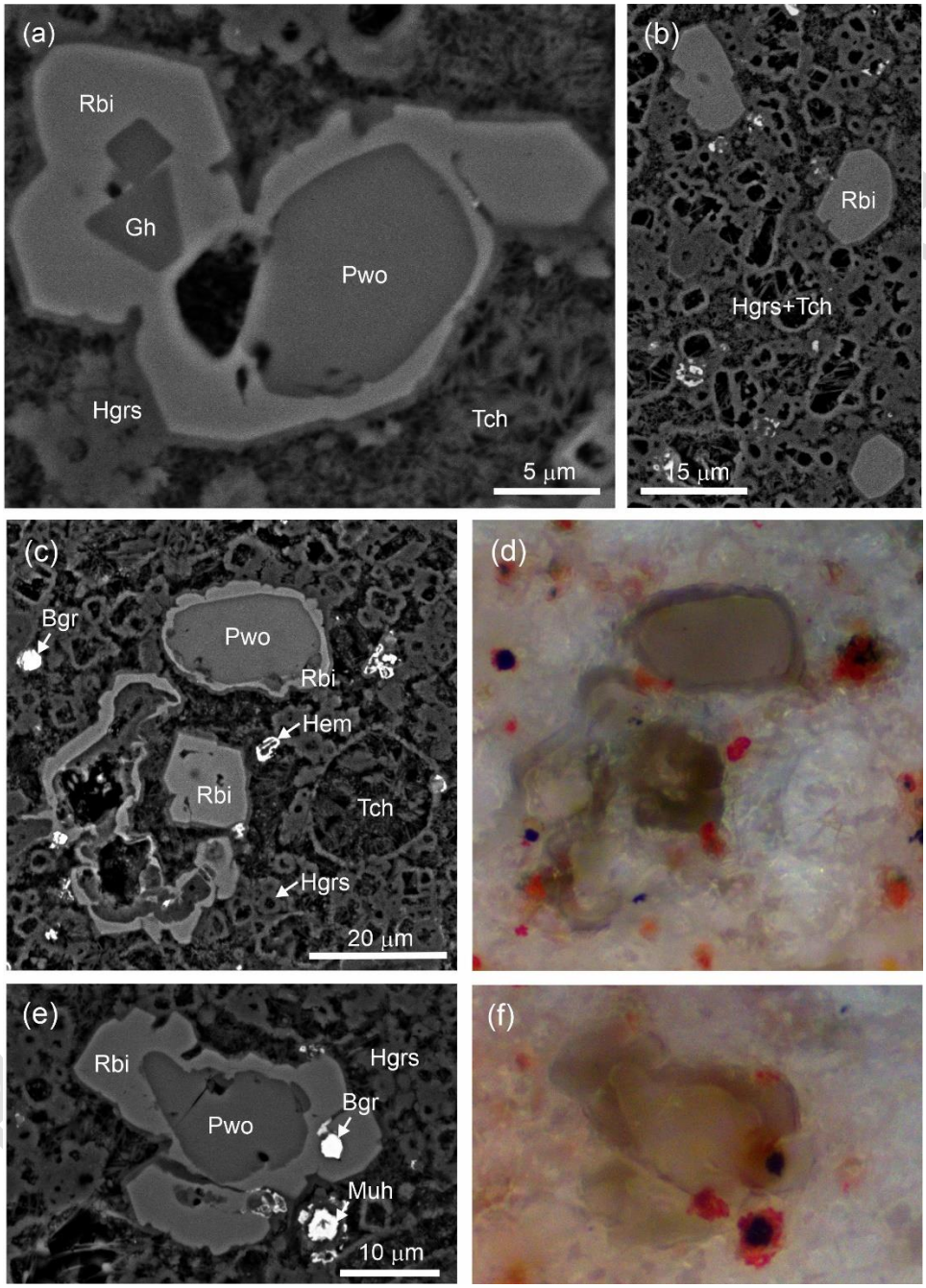

Figure 4. (a) Pseudowollastonite and gehlenite inclusions in rubinite, BSE. (b) Rare single crystals of rubinite with {221} faces, BSE. (c-f) – Reaction rim of rubinite on pseudowollastonite. c, e – BSE; d, f – Reflected light, XPL. Bgr = barringerite, Gh = gehlenite, Hem = hematite, Hgrs = hydrogrossular, Muh = murashkoite, Pwo = pseudowollastonite, Rbi = rubinite, Tch = tacharanite.

https://doi.org/10.1180/mgm.2025.3 Published online by Cambridge University Press

In one case, aggregates of garnet crystals of the grossular-rubinite series were found at the boundary between zones 2 and 3 (Fig. 5a,b). Garnet crystals occur in fragments of phosphide-rich rock and are associated with cuspidine, pseudowollastonite, and paqueite (Fig. 5c), rarely with unusual blue Ti^{3+}-bearing perovskite. Rubinite crystals overgrow a core of titanium-bearing grossular (Fig. 5d,e).

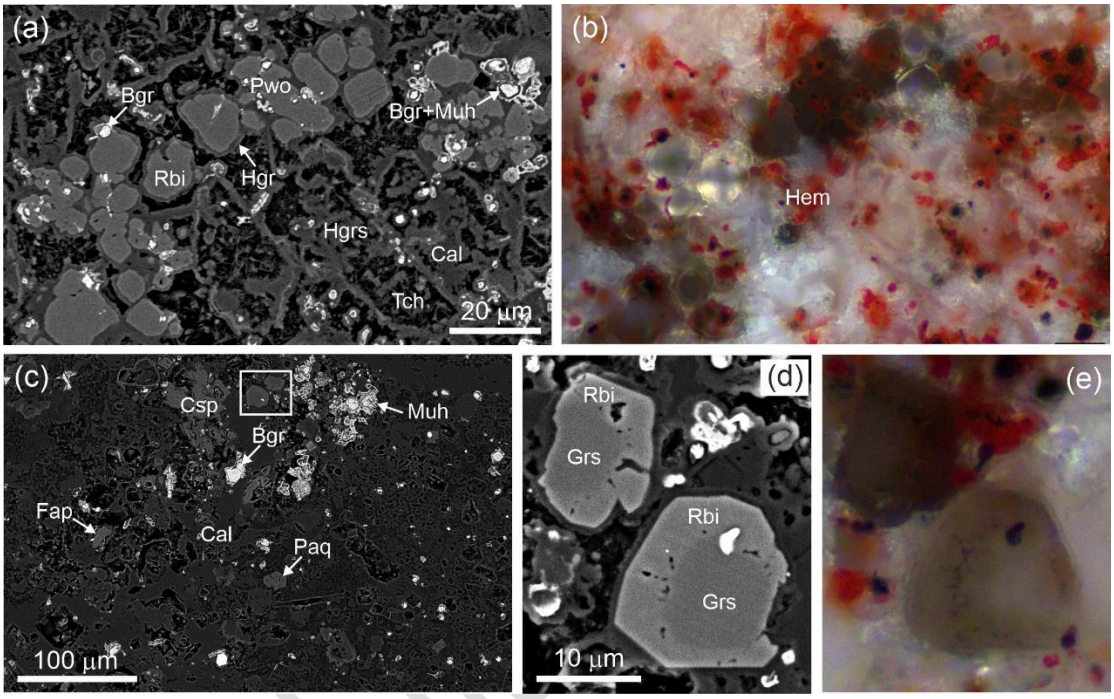

Figure 5. (a,b) Rare aggregates of garnet grains of the rubinite – grossular series from the boundary between paralava and xenolith (2 and 3 zones). a – BSE, b – Reflected light, XPL. (c) Position of zoned garnet crystals associated with phosphides and paqueite in the rock. Fragments magnified in Fig. 5d, e are outlined by frames. (d, f) Zoned crystals with a Ti-bearing grossular core and Al-bearing rubinite rim. d – BSE, e – Reflected light, XPL. e – Bright-red hematite replaces troilite and phosphides. Bgr = barringerite, Cal = calcite, Csp = cuspidine, Grs = grossular, Fap = fluorapatite, Hgrs = hydrogrossular, Hem = hematite, Muh = murashkoite, Paq = paqueite, Pwo = pseudowollastonite, Rbi = rubinite, Tch = tacharanite.

Chemical composition of rubinite and associated minerals

The composition of rubinite forming a reaction rim on pseudowollastonite in zone 4 of the xenolith, as well as its rare single crystals, is described by the average empirical formula $(Ca_{2.97}Mg_{0.02}Fe^{2+}_{0.01})_{\sum 3.00}(Ti^{3+}_{1.10}Al_{0.44}Ti^{4+}_{0.37}Mg_{0.08}Cr_{0.01})_{\sum 2}(Si_{2.71}Al_{0.29})_{\sum 3.00}O_{12}$ (Table 1, analysis 1), corresponding to 55% rubinite , 21% grossular, 14.5% hutcheonite and 8% Mg-analogue morimotoite end-members. Both in the reaction rims and in the central parts of individual crystals, small Al-enriched spots can be seen, distinguished on BSE images by their darker colour. In these spots, the content of the grossular end-member increases (30%) and the content of the rubinite end-member decreases (43%) (Table 1, analysis 2). The highest content of the rubinite end-member was found in the group of crystals shown in Fig. 3c (Table

https://doi.org/10.1180/mgm.2025.3 Published online by Cambridge University Press

2). One of the compositions of rubinite corresponds to the empirical formula $(Ca_{2.97}Mg_{0.03})_{\sum 3.00}(Ti^{3+}_{1.24}Ti^{4+}_{0.38}Al_{0.32}Mg_{0.05}Cr_{0.01})_{\sum 2}(Si_{2.66}Al_{0.34})_{\sum 3.00}O_{12}$, which is calculated to be 62% rubinite, 16% grossular, 17% hutcheonite and 5% Mg-analogue of morimotoite end-members.

Table 1. Chemical composition of rubinite in reaction zones on pseudowollastonite and single crystals (1) with dark spots (2) from zone 4 of the xenolith

	1			2		
Wt.%	n=71	s.d.	range	n=10	s.d.	range
ZrO_2	0.10	0.05	0-0.30	0.11	0.08	0-0.21
SiO_2	33.91	0.63	31.99-35.19	34.27	1.06	32.43-35.95
TiO_2*	6.22	0.84	4.41-9.02	6.74	1.39	4.68-9.11
Ti_2O_3*	16.40	0.94	14.06-18.48	13.04	0.43	12.21-13.65
Cr_2O_3	0.12	0.05	0-0.23	0.15	0.07	0-0.26
Al_2O_3	7.79	0.58	6.72-9.48	9.73	0.63	8.57-11.01
FeO	0.13	0.11	0-0.91	0.15	0.09	0-0.41
MgO	0.87	0.14	0.63-1.25	1.01	0.16	0.81-1.28
CaO	34.69	0.23	33.87-35.13	35.10	0.17	34.84-35.40
Na_2O	0.01	0.01	0-0.05	0.04	0.05	0-0.16
Total	100.24			100.33		
			Calculated on 12 O			
Ca apfu	2.97			2.97		
Fe^{2+}	0.01			0.01		
Na	0.00			0.01		
Mg	0.02			0.01		
X	3.00			3.00		
Ti^{3+}	1.10			0.86		
Al	0.44			0.61		
Ti^{4+}	0.37			0.40		
Cr	0.01			0.01		
Mg	0.08			0.12		
Y	2.00			2.00		
Si	2.71			2.71		
Al	0.29			0.29		
Z	3.00			3.00		
Rbi	55			43		
Grs	21			30		
Htn	14.5			14.5		
Mmt-Mg	8			12		
Ti^{4+}/Ti^{3+}	0.34			0.47		

* Ti^{3+}/Ti^{4+} ratio was calculated on charge balance
Rbi – $Ca_3Ti^{3+}_2Si_3O_{12}$, Grs – $Ca_3Al_2Si_3O_{12}$, Htn – $Ca_3Ti^{4+}_2(Al_2Si)O_{12}$, Mmt-Mg – $Ca_3MgTi^{4+}Si_3O_{12}$

The zoned garnet crystals forming aggregates at the boundary of zones 2 and 3 (Fig. 5c-e) have a core represented by a colourless Ti-bearing grossular with the empirical formula $(Ca_{2.97}Mg_{0.02}Fe^{2+}_{0.01})_{\sum 3.00}(Al_{0.85}Ti^{3+}_{0.68}Ti^{4+}_{0.33}Mg_{0.13}Cr_{0.01})_{\sum 2}(Si_{2.80}Al_{0.20})_{\sum 3.00}O_{12}$ (grossular 42.5%, rubinite 34%, hutcheonite 10% and Mg-analogue of morimotoite 13 %). The marginal zone of the crystals is formed by rubinite of dirty-green colour (Fig. 5d,e) with an average composition described by the empirical formula $(Ca_{2.96}Mg_{0.02}Fe^{2+}_{0.01}Na_{0.01})_{\sum 3.00}(Ti^{3+}_{1.00}$

https://doi.org/10.1180/mgm.2025.3 Published online by Cambridge University Press

$Ti^{4+}_{0.43}Al_{0.40}Mg_{0.15}Cr_{0.02})_{\sum 2}(Si_{2.74}Al_{0.26})_{\sum 3.00}O_{12}$ (rubinite – 50%, grossular – 20%, hutcheonite – 13% and Mg-analogue of morimotoite – 15%).

Table 2. Composition of rubinite shown in Fig. 3c (1) and Fig. 5d (2)

	Fig. 3c			Fig. 5d		
					core	rim
Wt.%	n=6	s.d.	range	n=1	n=5	n=4
ZrO_2	0.08	0.05	0.00-0.14	0.10	n.d.	n.d.
SiO_2	33.81	0.75	32.86-34.93	33.13	35.94	34.38
TiO_2*	6.14	0.57	5.11-6.96	6.32	5.59	7.10
Ti_2O_3*	16.96	1.47	14.33-18.48	18.48	10.35	15.01
Cr_2O_3	0.17	0.04	0.10-0.23	0.18	0.11	0.25
Al_2O_3	7.71	0.83	6.80-9.01	6.99	11.45	7.03
FeO	0.08	0.06	0-0.17	0.00	0.17	0.21
CaO	34.57	0.12	34.44-34.83	34.52	35.50	34.73
MgO	0.87	0.18	0.63-1.11	0.63	1.30	1.47
Na_2O	0.02	0.01	0-0.03	0.00	n.d.	0.04
Total	100.38			100.36	100.42	100.18
Ca apfu	2.96			2.97	2.97	2.96
Fe^{2+}	0.01				0.01	0.01
Na						0.01
Mg	0.03			0.03	0.02	0.02
X	3.00			3.00	3.00	3.00
Ti^{3+}	1.13			1.24	0.68	1.00
Al	0.42			0.32	0.85	0.40
Cr^{3+}	0.01			0.01	0.01	0.02
Ti^{4+}	0.37			0.38	0.33	0.43
Zr						
Mg	0.07			0.05	0.13	0.15
Y	2.00			2.00	2.00	2.00
Si	2.70			2.66	2.80	2.74
Al	0.30			0.34	0.20	0.26
Z	3.00			3.00	3.00	3.00
Rbi	56.5			62	34	50
Grs (+Prp)	21			16	42.5	20
Htn	15			17	10	13
Mmt-Mg	7			5	13	15
Ti^{4+}/Ti^{3+}	0.33			0.31	0.49	0.43

* Ti^{3+}/Ti^{4+} ratio was calculated on charge balance

Rbi – $Ca_3Ti^{3+}_2Si_3O_{12}$, Grs – $Ca_3Al_2Si_3O_{12}$, Htn – $Ca_3Ti^{4+}_2(Al_2Si)O_{12}$, Mmt-Mg – $Ca_3MgTi^{4+}Si_3O_{12}$

https://doi.org/10.1180/mgm.2025.3 Published online by Cambridge University Press

The diagram rubinite – grossular – hutcheonite + Mg-analogue of morimotoite shows the distribution of the garnet compositions, the overwhelming majority of which fall into the rubinite field (Fig. 6). Two trends in garnet composition can be observed: 1) $Grs_{42.5}Rbi_{34}Mmt\text{-}Mg_{13}Htn_{10} \rightarrow Rbi_{50}Grs_{20}Mmt\text{-}Mg_{15}Htn_{13}$ and 2) $Rbi_{43}Grs_{30}Htn_{14.5}$ Mmt-$Mg_{12} \rightarrow Rbi_{55}Grs_{21}Htn_{14.5}Mmt\text{-}Mg_{8}$. Both trends are accompanied by a decrease in the calculated Ti^{4+}/Ti^{3+} value.

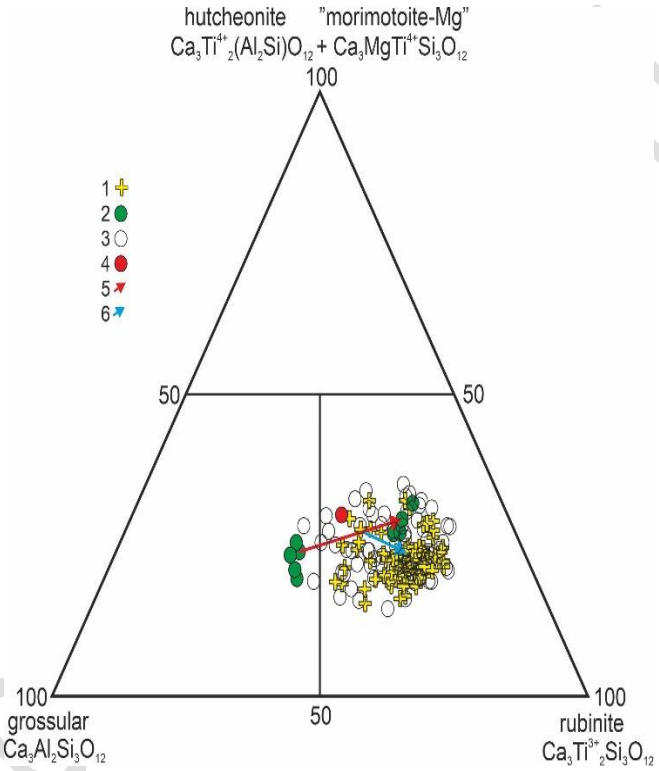

Figure 6. Garnet compositions plotted in the triangular diagram rubinite – grossular – hatcheonite + Mg-analogue of morimotoite. 1 – rubinite from zone 4; 2 – zoned garnet from the boundary of zones 2 and 3; 3 – EDS analyses; 4 – EDS analysis of crystal used for the structural study; 5, 6 – compositional trends .

The composition of relict high-temperature minerals and hydrogrossular associated with rubinite is given in Table 3. Paqueite from zone 3 of the xenolith (Table 3, analysis 1) is, like rubinite, a silicate of calcium, titanium and aluminium, but unlike the garnet it contains only Ti^{4+}: $(Ca_{2.97}Sr_{0.02}Na_{0.01})_{\sum 3.00}(Ti^{4+}_{0.97}Mg_{0.02}\,Fe^{2+}_{0.01})_{\sum 1.00}Si_2(Al_{2.05}Ti^{4+}_{0.71}Si_{0.26})_{\sum 3.02}O_{14}$.

https://doi.org/10.1180/mgm.2025.3 Published online by Cambridge University Press

Table 3. Chemical composition of paqueite (1), cuspidine (2), pseudowollastonite (3), gehlenite inclusions in rubinite (4) and hydrogrossular (5).

	1			2			3			4	5
Wt.%	n=8			n=8			n=7			n=2	n=3
P_2O_5	n.d.			n.d.			n.d.			n.d.	0.10
ZrO_2	0.07	0.06	0.02-0.23	0.18	0.05	0.13-0.29	n.d.			n.d.	n.d.
SiO_2	25.04	0.50	24.44-25.78	32.27	0.25	31.75-32.67	50.88	0.90	48.20-52.27	25.85	24.28
TiO_2	24.82	0.36	24.26-25.49	n.d.			0.15	0.06	0.10-0.27	n.d.	0.19
Ti_2O_3	n.d.			0.67	0.25	0.22-1.00					
Al_2O_3	19.25	0.26	18.85-19.71	0.13	0.15	0.03-0.53	0.47	0.47	0.06-1.71	31.10	20.56
Fe_2O_3											2.98
FeO	0.20	0.10	0.09-0.41	0.24	0.07	0.15-0.34	0.10	0.03	0.04-0.15	n.d.	
MgO	0.12	0.03	0.08-0.17	0.78	0.26	0.49-1.20	0.03	0.03	0.01-0.10	1.58	0.21
CaO	30.75	0.58	29.93-31.90	58.44	0.82	56.77-59.54	47.72	0.32	47.12-48.27	40.10	37.89
SrO	0.37	0.14	0.20-0.60	0.24	0.16	0.08-0.59	n.d.			n.d.	n.d.
Na_2O	0.03	0.03	0.01-0.09	0.12	0.02	0.10-0.17	0.02	0.01	0.00-0.04	0.37	0.05
Cl	n.d.			n.d.			n.d.			0.00	0.62
F	n.d.			10.35	0.22	9.71-10.52	n.d.			0.00	0.57
H_2O*											9.24
-O=F+Cl				2.33							0.39
Total	100.66			101.09			99.37			99.00	96.20
Ca	2.97[1]			3.85[2]			1.00[3]			1.97[4]	2.97[5]
Mg	0.02			0.07						0.11	0.02
Sr	0.02			0.01							
Na	0.01			0.01						0.03	0.01
Ti^{4+}	1.68			0.00							0.01
Ti^{3+}				0.03							
Fe^{3+}											0.16
Fe^{2+}	0.01			0.01							
Zr				0.01							
Al	2.05			0.01			0.01			1.68	1.77
Si	2.26			1.99			0.99			1.19	1.77
P^{5+}											0.01
Cl											0.08
F				2.01							0.13
OH											4.50

* – calculated, [1] – calculated on 14 O, [2] – calculated on 9(O+F), [3] – calculated on 3 O, [4] – calculated on 7 O; [5] – calculated on 12(O+OH+F+Cl) and normalised on 3(Ca+Mg+Na)

Raman spectra of rubinite

More than 30 Raman spectra have been obtained for rubinite, differing only in minor details. A typical rubinite spectrum is shown in Fig. 7, where there are bands corresponding to Si-O and Al-O vibrations in tetrahedra (TO_4) (Hofmeister and Chopelas, 1991; Makreski *et al.*, 2011) and weak bands related to Ti^{4+}-O vibrations in $(TiO_6)^{8-}$ octahedra appear: 610 cm^{-1} $\nu_1(TiO_6)^{8-}$ and 438 cm^{-1} $\nu_4(TiO_6)^{8-}$. In paqueite from the phosphide-bearing breccia these bands are at 611 and 437 cm^{-1}, respectively (Galuskina *et al.*, 2023). A shoulder at 765 cm^{-1} may correspond to the vibration $\nu_1(TiO_4)^{4-}$. The Raman spectrum of terrestrial rubinite is similar to that of the holotype rubinite from the meteorite (Ma *et al.*, 2024).

https://doi.org/10.1180/mgm.2025.3 Published online by Cambridge University Press

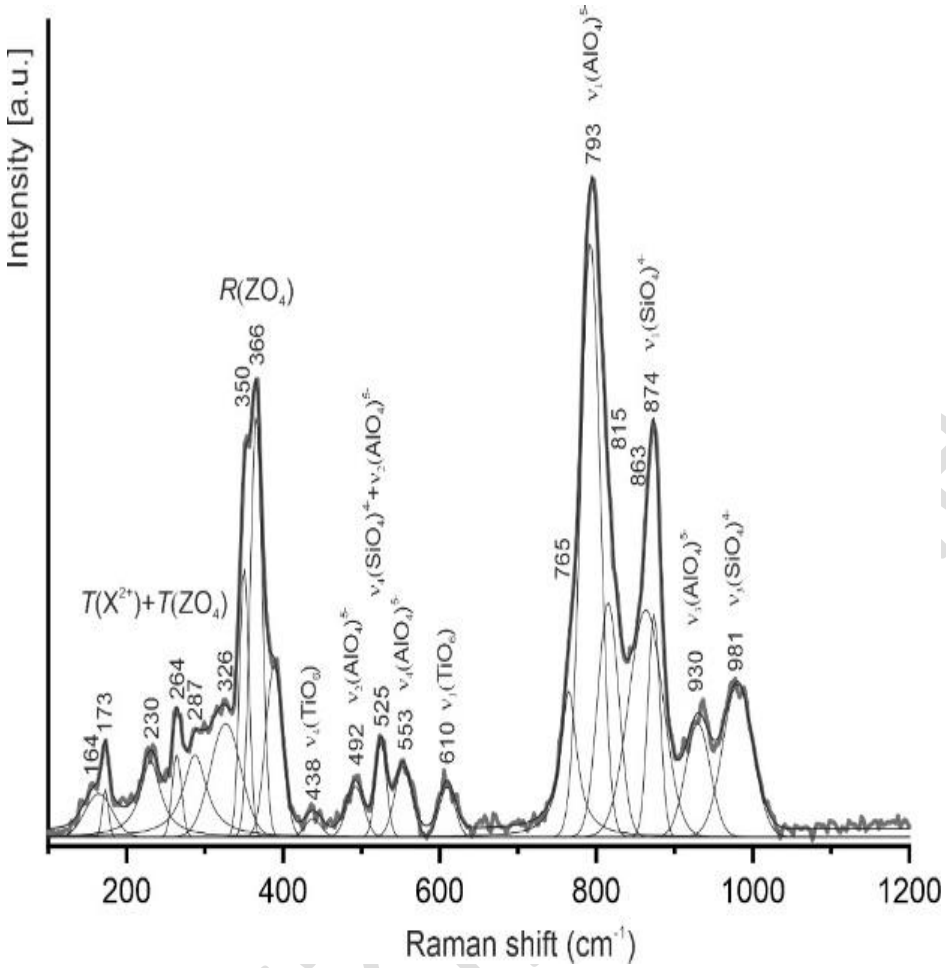

Figure 7. Raman spectrum of rubinite from the Hatrurim Complex.

Results of the study and discussion of the structure of rubinite

A fragment of the rubinite crystal 18 × 11× 9 μm in size from zone 4 was used for the single-crystal structure study. The average composition of this fragment according to the EDS data (mean 12) corresponds to the formula $(Ca_{2.99}Mg_{0.01})_{\Sigma 3}(Ti^{3+}_{0.78}Al_{0.62}Ti^{4+}_{0.43}Mg_{0.17})_{\Sigma 2}(Si_{2.74}Al_{0.26})_{\Sigma 3}O_{12}$, and in the diagram "rubinite – grossular – hatcheonite+Mg-analogue of morimotoite", its composition plots in the rubinite field (Fig. 6). The experimental details and refinement data for rubinite are summarised in Tables 4, 5.

https://doi.org/10.1180/mgm.2025.3 Published online by Cambridge University Press

Table 4. Crystal data and structure refinement details for rubinite

Crystal data	
Formula from refinement	$Ca_3(Ti_{0.577}Al_{0.40})_2Si_3O_{12}$
Crystal system	cubic
Space group	*Ia*3*d* (no. 230)
Unit-cell dimensions	*a* = 12.0193(4) *V* = 1736.35(9)Å^3
Z	8
Crystal size	0.018×0.011×0.009 mm
Data collection	
Diffractometer	SuperNova with Atlas CCD
Radiation wavelength	CuKα, λ = 1.54184 Å
Min. & max. theta	9.04°, 72.88°
Reflection ranges	-11 ≤ *h* ≤ 14; -14 ≤ *k* ≤ 13; -14≤ *l* ≤ 14
Refinement of structure	
Reflection measured	5214
No. of unique reflections	151
No. of observed unique refl. [*I*>3σ(*I*)]	119
Refined parameters	19
Rint	0.0559
R_1 / R_{all}	0.0256/0.0330
w*R*	0.0769
Goof	1.124
$\Delta\rho_{min}$ [e Å^{-3}]	-0.405
$\Delta\rho_{max}$ [e Å^{-3}]	0.315

Table 5. Atomic coordinates and isotropic displacement parameters (Å^2), anisotropic displacement parameters (Å^2), selected bond lengths (Å) and BVS calculation for rubinite

site	atom	*x*	*y*	*z*	U_{iso}*/U_{eq}	Occ.
*Ca*1	Ca	0.125	0	0.25	0.01673(18)	1
*Ti*1	Ti	0	0	0	0.0144(3)	0.577(3)Ti+0.4Al
*Si*1	Si	0.375	0	0.25	0.0136(2)	1
*O*1	O	-0.20306(10)	0.21120(11)	0.09611(9)	0.0191(3)	1
site	U^{11}	U^{22}	U^{33}	U^{23}	U^{13}	U^{12}
*Ca*1	0.0152(3)	0.0175(2)	0.0175(2)	0.0020(2)	0	0
*Ti*1	0.0144(3)	0.0144(3)	0.0144(3)	0.0002(3)	0.0002(3)	0.0002(3)
*Si*1	0.0128(4)	0.0139(3)	0.0139(3)	0	0	0
*O*1	0.0188(6)	0.0193(5)	0.0191(6)	0.0019(5)	-0.0012(5)	0.0000(5)
Atom	-atom			BVS	Formula charge	
*Ca*1	-O1	2.3513(12)	×4	2.31	2	
	-O1	2.5089(12)	×4			
	sum	2.430				
*Ti*1	-O1	1.9893(11)	×6	3.09	3.13	
*Si*1	-O1	1.6510(12)	×4	3.83	3.91	
*O*1				2.02	2	

Rubinite belongs to the garnet supergroup. Its structure is formed by zigzag columns consisting of X polyhedra and Y octahedra with Si tetrahedra between them (Grew *et al.*,

https://doi.org/10.1180/mgm.2025.3 Published online by Cambridge University Press

2013; Fig. 8). The 8-coordinate X site is occupied by Ca, mean distance Ca-O = 2.43 Å. At the tetrahedral Z site there is Si and a small amount of Al, Z-O distance = 1.651Å. At the octahedral Y site there are four types of cations, $Ti^{3+}_{0.78}Al_{0.62}$ $Ti^{4+}_{0.43}Mg_{0.17}$, whose ionic radii are 0.670, 0.535, 0.605 and 0.72, respectively (Shannon, 1976). A theoretical calculation shows that a virtual cation with 18.4 e- should be at the Y-site and the Y-O distance is ~1.98 Å. The results of the structure refinement give the close matches: 17.89 e- and Y-O = 1.989 Å (Table 4).

Terrestrial rubinite has an *a* unit-cell parameter equal to 12.0193(4) Å. The synthetic analogue, informally named "imanite", whose structure was used as a model during the EBSD study of meteoritic rubinite, has a significantly larger parameter *a* = 12.1875(2) Å (Valldor *et al*., 2011). A difference in the ionic radii Cr^{3+} = 0.615 and V^{3+} = 0.64 is insignificant, corresponding to a slight difference in the parameters of uvarovite $Ca_3Cr^{3+}_2Si_3O_{12}$, *a* =11.988(1) Å, and goldmanite, $Ca_3V^{3+}_2Si_3O_{12}$, *a* = 12.011(1) Å (Novak and Gibbs, 1971). The radius of Ti^{3+} = 0.67 is slightly larger than the ionic radii of Cr^{3+} and V^{3+}, but the parameter of the synthetic $Ca_3Ti^{3+}_2Si_3O_{12}$ is unexpectedly large *a* = 12.1875 Å. We believe that the parameter *a* of rubinite from meteorite should be much smaller, since the Y-O distance ≈ 2.01 Å calculated using the composition (Ma *et al*., 2024) is only slightly larger than the distance of Y-O ≈ 1.98 Å calculated for terrestrial rubinite.

We have studied Fe-free uvarovite from paralava containing native iron from the Hatrurim Complex; its empirical formula is $Ca_{3.00}(Cr^{3+}_{1.24}Al_{0.36}Ti^{4+}_{0.22}V^{3+}_{0.14}Fe^{2+}_{0.02}Mg_{0.02})_{\sum 2.00}(Si_{2.85}Al_{0.15})_{\sum 3}O_{12}$ and it has an *a* parameter equal to 12.0253(3) Å, which is close to that of terrestrial rubinite, and similar interatomic distances in polyhedra (Futrzyński *et al*., 2023; Fig. 8C, B), so the structure of uvarovite was used as a starting model during the structure refinement of rubinite.

It is interesting to note that there is overbonding at the *X* site in rubinite (2.31 v.u. = valence unit) (Table 4) and other calcium garnets, such as uvarovite (2.34), grossular (2.52 v.u.), schorlomite (2.27 v.u.) and goldmanite (2.37 v.u.), whereas for almandine (1.83 v.u.) insignificant underbonding of Fe^{2+} at the X site is observed (structural data from Novak and Gibbs, 1971; Futrzyński *et al*., 2023). The geometry of Ca sites is determined by the 3D framework consisting of alternating Z- tetrahedra and Y-octahedra with shared corners.

https://doi.org/10.1180/mgm.2025.3 Published online by Cambridge University Press

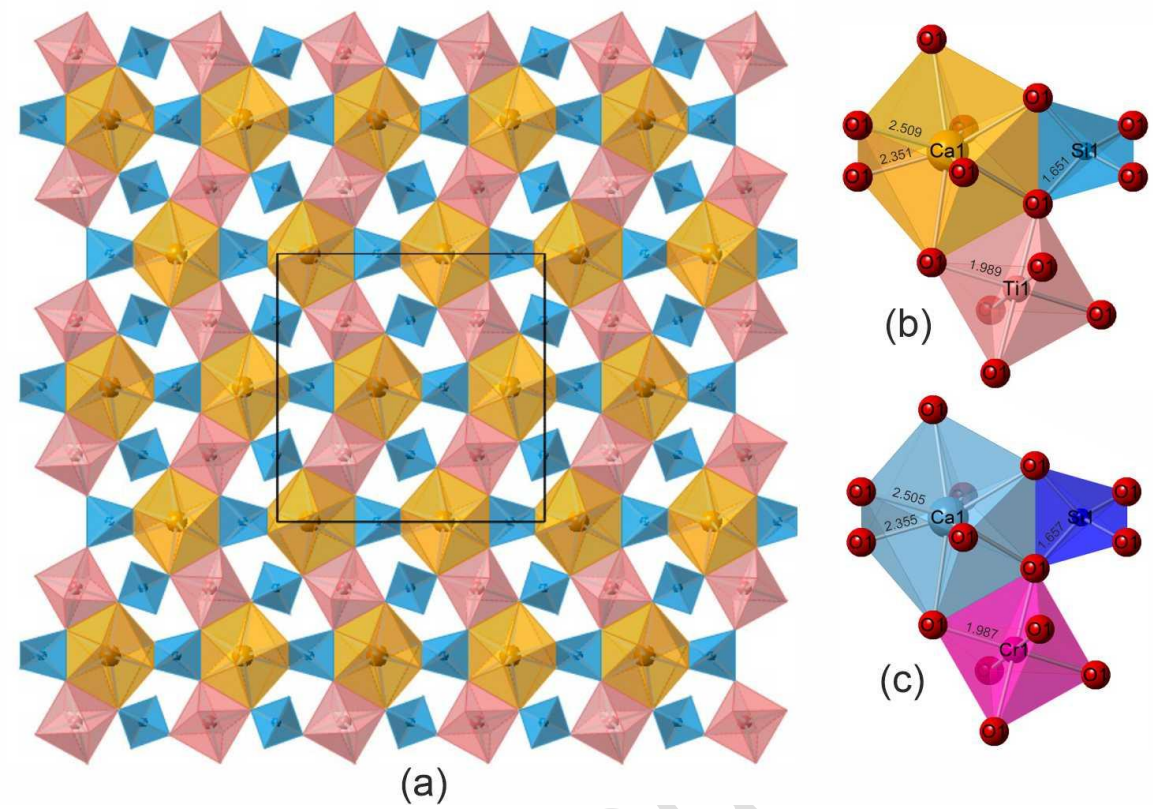

Figure 8. (a) A layer of the rubinite structure. Between zigzag columns composed of Ca-polyhedra and Ti-octahedra there are TO_4 tetrahedra. The black frame shows the unit cell. (b) and (c) Fragments of rubinite and Fe-free uvarovite structures, respectively, with similar interatomic distances.

The genesis of rubinite

The formation of rubinite is induced by high-temperature processes during the interaction of hot paralava generated at temperatures above 1,200°C with the thermally altered fragments of carbonate-clay sedimentary rocks of the Ghareb Formation (Galuskin *et al.*, 2022, 2023). Geochemical data suggest that the carbonate-clay sedimentary rock was a protolith of the paralava that cemented its clinkerised fragments (Galuskin *et al.*, 2022). Preliminary thermal alteration of the sedimentary rocks caused graphitisation of fish bone remains and replacement of numerous framboids by hematite (Galuskin *et al.*, 2024) This was a necessary condition for the realisation of carbothermal reduced reactions at the contact of the hot paralava, leading to the mass formation of phosphide and native iron aggregates as well as osbornite (Galuskin *et al.*, 2022, 2023). Interestingly, osbornite and phosphides were also detected as micrometric inclusions within small xenoliths (up to a few cm in size). Thermal alteration of the xenoliths caused their partial melting and contamination by the paralava, resulting in the formation of a paralava contact facies enriched in pseudowollastonite and phosphides (Galuskin *et al.*, 2023). This process was accompanied by the formation of small droplets of melt within the xenolith, from which Ca-silicates (pseudowollastonite and cuspidine) and phosphides formed. The fine-grained porous clinker

https://doi.org/10.1180/mgm.2025.3 Published online by Cambridge University Press

matrix of the xenolith was mainly represented by gehlenite and hatrurite aggregates, probably with an impurity of oldhamite, lime and minerals of the mayenite group. At the contact with the paralava, two processes related to xenolith melting are observed: contamination of the paralava with xenolith material and formation of a thin "melted zone" of the xenolith itself (Fig. 1a,b). Paqueite, in contrast to rubinite, which is located in the central part of the xenolith, crystallized only in the xenolith melting zone (zone 3) and, in contrast to rubinite and its meteoritic analogue, does not contain any Ti^{3+} (Fig. 1f; 2a,d; 5c; Table 3, analysis 1). Paqueite formation can be represented by the following reaction: $CaSiO_3$ (pseudowollastonite) + $Ca_2Al_2SiO_7$ (gehlenite) + $2TiO_2$ (rutile) = $Ca_3Ti^{4+}(Al_2Ti^{4+})Si_2O_{14}$ (paqueite). The majority of rubinite grains form a rim on pseudowollastonite, probably at the moment of an abrupt increase in the porosity of the xenolith during the progressive process of clinkerisation. The high porosity of the rocks led to an increase in the activity of reducing gases and the formation of the Ti^{3+}-bearing minerals osbornite and rubinite (Fig. 3d,e). Rubinite was formed by the reaction $3CaSiO_3$ (pseudowollastonite) + Ti_2O_3 (tistarite) = $Ca_3Ti^{3+}{}_2Si_3O_{12}$ (rubinite). The reduction of Ti was a carbothermic reaction due to the carbon released as a result of the decomposition of the graphitised fish bone remains: $2Ti^{4+}O_2$ + C/CO = $Ti^{3+}{}_2O_3$ + CO/CO_2. Thus, it is possible to follow a decrease in oxygen activity in the direction from the paralava (close to the Fe/FeO buffer, $\Delta IW \approx 0$) through the contact zone with phosphides ($\Delta IW \approx -3 – -4$) towards the central parts of the xenolith ($\Delta IW \approx -7 – -8$). The heterogeneity of the rocks and the involvement of gases would have disrupted this regularity, which is confirmed by the finding of rare aggregates of rubinite crystals with a grossular core formed at the boundary of the contact facies of the paralava contaminated by xenolith materials and the "melted zone" of the xenolith (Fig. 5).

Rubinite found *in situ* from phosphide-bearing breccia of the Hatrurim Complex. Rubinite is at present the only authentic silicate with trivalent titanium formed on Earth under super-reduced conditions.

Acknowledgments: The authors thank the three anonymous reviewers, the Technical Editor, the Associate Editor Robert Martin, and the Principal Editor Stuart Mills for remarks and comments that improved an earlier version of the manuscript. Investigations were partially supported by the National Science Centre of Poland, Grant No. 2021/41/B/ST10/00130. This paper is dedicated to Edward Sturgis Grew on the occasion of his 80th birthday.

https://doi.org/10.1180/mgm.2025.3 Published online by Cambridge University Press

References

Ballhaus, C., Helmy, H.M., Fonseca, R.O.C., Wirth, R., Schreiber, A. and Jöns, N. (2021) Ultra-reduced phases in ophiolites cannot come from Earth's mantle. *American Mineralogist*, **106**, 1053–1063.

Futrzyński, J., Juroszek, R., Skrzyńska, K., Vapnik, Y. and Galuskin, E. (2023) Uvarovite from reduced native Fe-bearing paralava, Hatrurim Complex, Israel. *Lithosphere*, **2023**, lithosphere_2023_214.

Galuskin, E. and Galuskina, I. (2023a) Evidence of the anthropogenic origin of the 'Carmel sapphire' with enigmatic super-reduced minerals. *Mineralogical Magazine*, **87**, 619–630.

Galuskin, E. and Galuskina, I. (2023b) Reply to the discussion of Galuskin and Galuskina (2023) " *Evidence of the anthropogenic origin of the 'Carmel sapphire' with enigmatic super-reduced minerals* " by Griffin *et al* . (2023). *Mineralogical Magazine*, **87**, 635–638.

Galuskin, E., Galuskina, I.O., Kamenetsky, V., Vapnik, Y., Kusz, J. and Zieliński, G. (2022) First *in situ* terrestrial osbornite (TiN) in the pyrometamorphic Hatrurim Complex, Israel. *Lithosphere*, **2022**, 8127747.

Galuskin, E., Galuskina, I., Vapnik, Y., Kusz, J., Marciniak-Maliszewska, B. and Zieliński, G. (2024) Two modes of terrestrial phosphide formation. *American Mineralogist*, https://doi.org/10.2138/am-2024-9315.

Galuskin, E.V., Galuskina, I.O., Vapnik, Y. and Zieliński, G. (2023a) Discovery of "meteoritic" layered disulphides $ACrS_2$ (A = Na, Cu, Ag) in terrestrial rock. *Minerals*, **13**, 381.

Galuskin, E.V., Kusz, J., Galuskina, I.O., Książek, M., Vapnik, Y. and Zieliński, G. (2023b) Discovery of terrestrial andreyivanovite, FeCrP, and the effect of Cr and V substitution on the low-pressure barringerite-allabogdanite transition. *American Mineralogist*, **108**, 1506–1515.

Galuskina, I., Galuskin, E., Vapnik, Y., Zeliński, G. and Prusik, K. (2021) Priscillagrewite-(Y), $(Ca_2Y)Zr_2Al_3O_{12}$: A new garnet of the bitikleite group from the Daba-Siwaqa area, the Hatrurim Complex, Jordan. *American Mineralogist*, **106**, 641–649.

Galuskina, I., Galuskin, E. and Vapnik, Y. (2023) Not only garnets…. *Lithosphere*, **2023**, lithosphere_2023_186.

Grew, E.S., Locock, A.J., Mills, S.J., Galuskina, I.O., Galuskin, E.V. and Halenius, U. (2013) Nomenclature of the garnet supergroup. *American Mineralogist*, **98**, 785–811.

https://doi.org/10.1180/mgm.2025.3 Published online by Cambridge University Press

Griffin, W., Gain, S., Bindi, L., Toledo, V., Cámara, F., Saunders, M. and O'Reilly, S. (2018) Carmeltazite, $ZrAl_2Ti_4O_{11}$, a new mineral trapped in corundum from volcanic rocks of Mt Carmel, Northern Israel. *Minerals*, **8**, 601.

Griffin, W.L., Gain, S.E.M., Adams, D.T., Huang, J.-X., Saunders, M., Toledo, V., Pearson, N.J. and O'Reilly, S.Y. (2016) First terrestrial occurrence of tistarite (Ti_2O_3): Ultra-low oxygen fugacity in the upper mantle beneath Mount Carmel, Israel. *Geology*, **44**, 815–818.

Hofmeister, A.M. and Chopelas, A. (1991) Vibrational spectroscopy of end-member silicate garnets. *Physics and Chemistry of Minerals*, **17**, 503-526.

Kruszewski, Ł., Palchik, V., Vapnik, Y., Nowak, K., Banasik, K. and Galuskina, I. (2021) Mineralogical, geochemical, and rock mechanic characteristics of zeolite-bearing rocks of the Hatrurim Basin, Israel. *Minerals*, **11**, 1062.

Krzątała, A., Krüger, B., Galuskina, I., Vapnik, Y. and Galuskin, E. (2020) Walstromite, $BaCa_2(Si_3O_9)$, from rankinite paralava within gehlenite hornfels of the Hatrurim Basin, Negev Desert, Israel. *Minerals*, **10**, 407.

Litasov, K.D., Kagi, H. and Bekker, T.B. (2019) Enigmatic super-reduced phases in corundum from natural rocks: Possible contamination from artificial abrasive materials or metallurgical slags. *Lithos*, **340–341**, 181–190.

Ma, C., Yoshizaki, T., Krot, A.N., Beckett, J.R., Nakamura, T., Nagashima, K., Muto, J., Ivanova, M.A. and Ulyanov, A.A. (2025) Rubinite, $Ca_3Ti^{3+}{}_2Si_3O_{12}$, a new mineral in CV3 carbonaceous chondrites and a refractory garnet from the solar nebula. *American Mineralogist*, https://doi.org/10.2138/am-2024-9435.

Makreski, P., Runčevski, T. and Jovanovski, G. (2011) Minerals from Macedonia. XXVI. Characterization and spectra–structure correlations for grossular and uvarovite. Raman study supported by IR spectroscopy. *Journal of Raman Spectroscopy*, **42**, 72–77.

Novak, G.A., Gibbs, G.V. (1971) The crystal chemistry of the silicate garnets. *American Mineralogist*, **56**, 791–825.

Shannon, R.D. (1976) Revised effective ionic radii and systematic studies of interatomic distances in halides and chalcogenides. *Acta Crystallographica Section A*, **32**, 751–767.

Sheldrick, G.M. (2015) Crystal structure refinement with *SHELXL*. *Acta Crystallographica Section C Structural Chemistry*, **71**, 3–8.

Valldor, M., Uthe, A. and Rückamp, R. (2011) Antiferromagnetic ground state of quantum spins in the synthetic imanite, $Ca_3Ti_2Si_3O_{12}$: The lost child of the garnet family. *Inorganic Chemistry*, **50**, 10107–10112.

https://doi.org/10.1180/mgm.2025.3 Published online by Cambridge University Press